Poling thin-film x-cut lithium niobate for quasi-phase matching with sub-micrometer periodicity

Jie Zhao,[1, a)] Michael Rüsing,[1, 2, b)] Matthias Roeper,[2] Lukas M. Eng,[2] and Shayan Mookherjea[1]
[1)]*Department of Electrical and Computer Engineering, University of California, San Diego, 9500 Gilman Drive, La Jolla, CA 92093-0407, USA*
[2)]*TU Dresden, Institut für Angewandte Physik, Nöthnitzer Strasse 61, 01187 Dresden, Germany*

Quasi-phase-matched grating structures in lithium niobate waveguides with sub-micron periodicities will benefit the development of short-wavelength nonlinear optical devices. Here, we report on the reproducible formation of periodically-poled domains in x-cut single-crystalline thin-film lithium niobate with periodicities as short as 600 nm. Shaped single-voltage poling pulses were applied to electrode structures which were fabricated by a combination of electron-beam and direct-writing laser lithography. Evidence of successful poling with good quality was obtained through second-harmonic microscopy and piezoresponse force microscopy imaging. For the sub-micron period structures, we observed patterns with a double periodicity formed by domain interactions, and features with sizes less than 200 nm.

I. INTRODUCTION

In certain optically-transparent ferroelectric crystals, the periodic inversion of the domain orientation along the length of a waveguide structure, known as quasi-phase matching (QPM), provides an additional k-vector to compensate for the phase mismatch between the nonlinear optical interaction of the pump, signal and idler optical waves. When allowed by the material and the fabrication techniques, QPM provides considerable freedom for the designer by optimizing the waveguide properties, such as the mode cross-section, the mode dispersion, and polarization properties. This often makes QPM the preferred approach over traditional phase matching methods, such as angular tuning in bulk crystals or birefringent phase-matching in multi-mode waveguides, which are limited in interaction length. Notably, the ability to achieve QPM between counter-propagating waves is essential to the realization of a mirrorless optical parametric oscillator (OPO), as has been demonstrated in periodically-poled $KTiOPO_4$ (PPKTP)[1], but not yet in periodically-poled lithium niobate (PPLN). In fact, a poling period (Λ) of 600 nm or less has been calculated for first-order phase matching in bulk PPLN waveguides[2]; the fabrication of homogeneous periodic domain structures with such deeply-sub-micron periodicities that penetrate across the complete waveguide modal area has not yet been achieved.

In LN, poling is most commonly achieved by the application of a strong electric field along the ferroelectric z axis of the crystal. During the electric field poling process, new domains nucleate at the poling electrodes and predominantly grow along the z axis (forward growth), while at the same time spread laterally. While sub-micron domain periods have been achieved in bulk LN with this method, the depth of these domain structures are shallow when compared to the usual depth of waveguides formed in bulk LN (5-10 μm)[3–5]. Furthermore, achieving sub-micron QPM periods in bulk LN often requires sophisticated fabrication protocols[6], while for larger periods standard lithography process is appropriate. The realization of domain structures with sub-micron periodicity which is shown in LN is also achievable in KTP[7–10]. Depending on the wavelength of interest, LN has higher nonlinear optical coefficients[11] and is available in larger wafer sizes (up to 6 inches) which may benefit the development of practical photonic devices. Moreover, LN is of considerable interest for device development because it is also widely used for optical modulators, acoustic wave filters, and memory devices[12–16]. Over the last decade, single crystalline thin films of LN (TFLN) have become available on common handle wafers (quartz, silicon or lithium niobate). The small thickness and the high index contrast of LN on an oxide buffer layer enable the formation of waveguides with sub-wavelength modal area and tight bending radius, compared to the traditional Ti in-diffused or proton exchanged waveguides in bulk LN. Such waveguides can support modes with similar cross-sectional profiles at widely separated wavelengths, which results in a highly efficient wavelength conversion device[17–22]. For periodic poling of z-cut TFLN, the thin-film structure promises much smaller domain periods, since the inverted domains might have a width as small as the film thickness, which is similar to the penetration depth of typical sub-micron domain structures that have been formed in bulk LN[3–5]. However, poling z-cut TFLN often requires buried electrodes[23], which is not favorable for low-loss optical waveguide applications due to the resulting presence of buried metal electrodes in the vicinity of the optical mode. Alternatively, the poling ground electrode can be formed at the backside of the chip handle, yet elevated poling temperature is needed to reduce the coercive field of LN and thus the poling voltage[24]. In contrast, x-cut (and y-cut) TFLN can be poled easily at room temperature using surface electrodes which can be removed after poling[25]. The electrodes can also be retained, if placed at a sufficient distance away from the waveguide region. Nevertheless, sub-micron poling of x-cut TFLN remains challenging at the present time, since narrow domains will spread and may merge before being completely inverted in depth. Therefore, the fabrication of uniform and completely inverted (in depth) domain structures requires careful optimization of the poling process, e.g., the electrode structures, poling pulse waveform,

[a)]Electronic mail: jiz378@eng.ucsd.edu
[b)]Electronic mail: michael.ruesing@tu-dresden.de

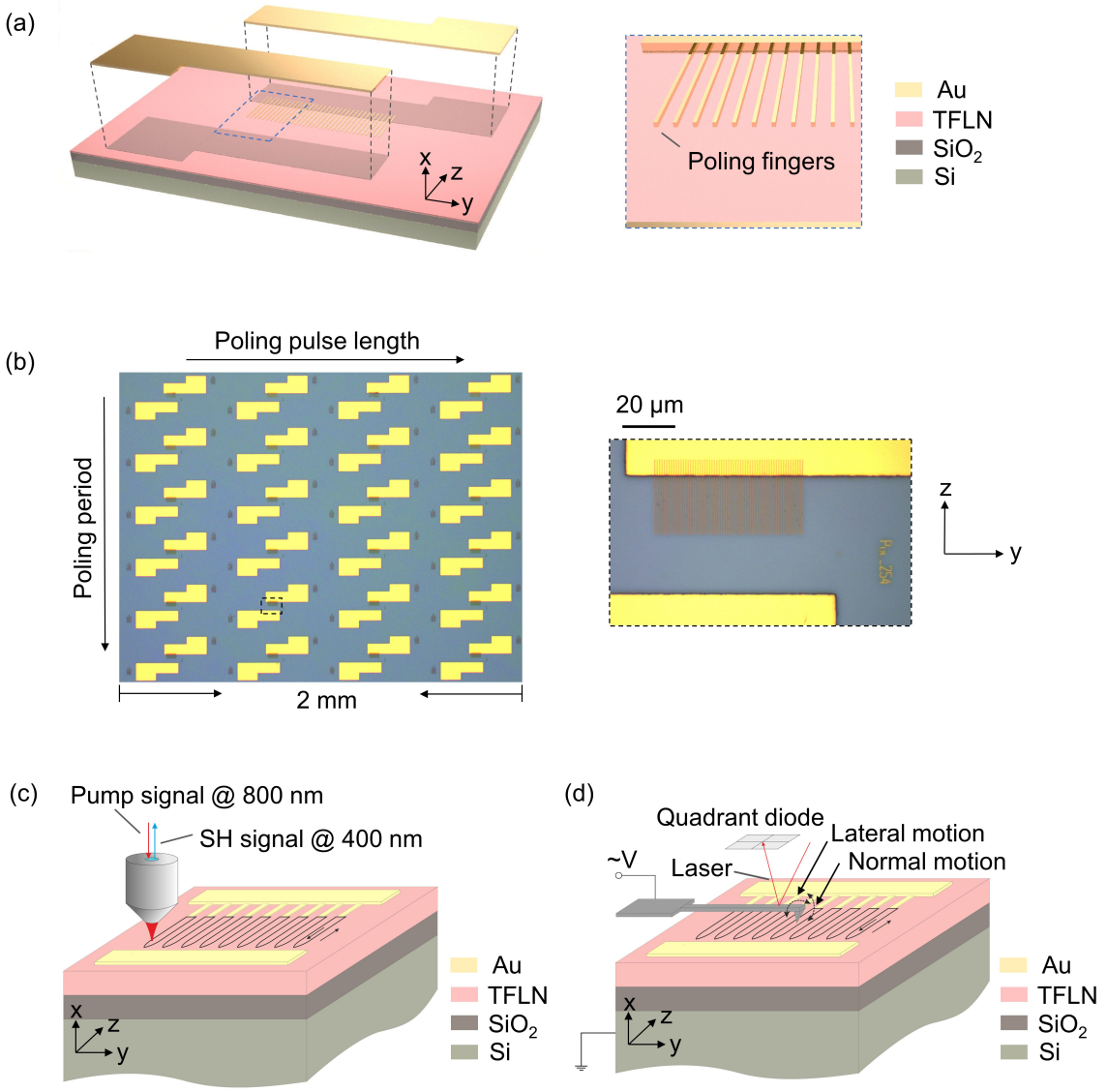

FIG. 1. (a) Exploded representation of the x-cut TFLN with surface electrodes for poling, where the thin poling finger electrodes were first fabricated using electron-beam lithography, and the thick probe contact pads were formed by photolithography subsequently. Inset shows the poling finger electrodes. (b) Microscope images of the fabricated device. As an example, inset shows one set of poling electrodes with a period of 800 nm. (c) and (d) Schematic illustrations of second-harmonic (SH) microscopy (c) and piezoresponse force microscopy (PFM) (d) imaging of the poled sample.

as well as development of non-destructive methods to characterize and study the domain structures.

Here, we show a systematic study of x-cut TFLN poling with periods varying from 2.8 μm to 600 nm, using standard poling electrodes and singe voltage pulses. Non-destructive second-harmonic (SH) microscopy was used here for domain visualization, which provides quick feedbacks on the poling fidelity and guidance for poling pulse optimization. Details of the sub-micron period domain structures were then examined with piezoresponse force microscopy (PFM). Domain grids with periods down to 600 nm were successfully fabricated, which extend in the z direction far enough to cover the TE_0 optical mode in typical TFLN waveguides. Poling with periods over such a wide range was achieved using the same protocol, with only slight modifications in pulse length or pulse height. Furthermore, we observed evidence of fully inverted domains (in-depth), rather than surface domains with periods down to 800 nm, which is critical to achieve efficient QPM devices.

II. METHOD

Based on the type of wafer that is useful for optical waveguide devices[26], we studied poling of 5 mol% magnesium oxide (MgO) doped, x-cut lithium niobate on insulator (LNOI), acquired from NanoLN (Jinan Jingzheng Electronics Co., Ltd.). The material stack for the LNOI chip is shown in

Fig. 1(a), which consists of a 300 nm-thick top functional layer (TFLN) and a 1.8 μm-thick buried oxide layer on a silicon handle. Test structures were fabricated with poling electrodes of 50 μm length and various periods ranging from 2 μm down to 600 nm [see Fig. 1(b)]. The separation gap between the two opposing electrode "teeth" facing each other was designed to be 20 μm, based on an estimate of the critical field required for initiating poling. The duty cycle of the patterned electrodes was fixed at 20%, to pre-compensate for the lateral spreading of the inverted domains; thus, photolithography provides insufficient resolution for defining the electrode structure accurately. On the other hand, electron-beam lithography alone is a relatively slow and serial-write process, not well suited to write large contact pads and long electrode structures that will eventually be needed. Thus, we developed a two-step lithography process using both photolithography and e-beam lithography. The latter was used first, to define the poling electrode "teeth" with high resolution, followed by the metal deposition (15 nm Cr/80 nm Au, deposited by electron-beam evaporation) and lift-off process. The probe contact pads were then aligned and structured by photolithography, together with a second metallization step and lift-off process. In cross-section, the contact pads consist of a 15 nm Cr adhesion layer and a 300 nm Au layer. As an example, the inset of Fig. 1(b) shows the microscope image of a set of fabricated poling electrodes with a period of 800 nm. A schematic illustration of the sample geometry is shown in Fig. 1(a). It should be noted that only the positive electrodes have been structured periodically, while the negative counter electrode is represented by a flat rectangle with no "teeth". During our experiments we found no significant differences when using either a flat or a structured ground electrode. Poling was performed by applying a single voltage pulse, with transformer oil surrounding the probe-pad contact point and the immediate vicinity of the electrodes, which helped prevent arcing and breakdown. As a starting point for the subsequent optimization, a standard poling voltage waveform was chosen here[27], i.e., an initial rapid ramp-up of the voltage to initiate the generation of nucleation sites, a hold of the voltage above the coercive field strength for about 1 ms, and then a slow ramp-down of the voltage to stabilize the newly-formed domains. Subsequently the sample was investigated with a second-harmonic microscopy setup, as is shown in Fig. 1(c). The poling pulse waveform, i.e., the length of the pulse or stabilization phase and the pulse height, was iteratively optimized for each period by imaging and re-poling. Details about the poling setup as well as waveform optimization can be found in the supplementary material.

As we have demonstrated in previous works and extensive simulations (see supplementary material), SH microscopy is sensitive to the depth of an inverted domain[28]. This can be easily understood if two domains of different orientation are stacked vertically, the SH signal generated in each of these vertically stacked domains will destructively interfere, leading to a decrease in the generated SH signal compared to that from a completely inverted or unpoled region. In the SH imaging process, both forward and backward-propagating phase-matched signals are generated. While for the backward phase-matched SH signal this cannot be observed, because the nonlinear coherent interaction length ($\approx$ 44 nm) is much smaller than the film thickness. However, the forward phase-matched signal has a nonlinear coherent interaction length (1.28 μm) larger than the film thickness, and thus because of the longer interaction length it is also two orders of magnitude stronger than the backward-generated signal. Furthermore, due to the highly reflective interfaces below the film, the strong forward signal can be observed in backward direction, i.e., in a reflection geometry microscope. As demonstrated by detailed simulations[28], for domains completely inverted in depth, the same SH signal will be detected from completely poled and unpoled regions. In a fully inverted domain, only the dark lines belonging to the domain transitions are expected to be seen, as is indicated in Fig. 1(c). However, although in SH images for structures with sub-micrometer periods, a periodic pattern can still be seen, the diffraction-limited resolution of SH microscopy ($\approx$ 310 nm for 800 nm pump wavelength and a numerical aperture of 0.9) masks further details of the poled domain structures. This is confirmed by the simulation results and SH images shown in the supplementary material. Therefore, the structures with periods of 1 μm and less have been analyzed with PFM. The PFM measurement was performed using a Cypher AFM (Asylum Research - Oxford instruments) in the built-in Vector-PFM mode, which allows recording of the lateral (torsion motion of the cantilever) and normal (deflection) PFM signals during the same scan, as is depicted in Fig. 1(d).

III. RESULTS

Figure 2 shows SH microscope images of domain structures with poling periods of 2.8 μm (a), 2 μm (b) and 1.5 μm (c). In order to create a typical 2D image, a selected region was scanned with 50 nm and 150 nm step width along the y and z axis of the TFLN respectively, and 5 ms signal integration time per acquisition point. The poling electrodes are visible as dark stripes and rectangles at the top and bottom of the image, because the electrode material (gold) features no second order nonlinearity in the optical band. The domain walls (DWs) appear as dark lines stretching from the positive to the negative electrodes and the bright regions surrounded by the DWs correspond to the inverted regions. The calculated duty cycles are 48.8% $\pm$ 1.5%, 44.3% $\pm$ 3.3% and 51.2% $\pm$ 4.2% for $\Lambda = 2.8$ μm, 2 μm and 1.5 μm respectively. This estimation is based on line-scans of the SH signal through the middle of the poling region over 20 periods. Down to the 1.5 μm period, as shown in Fig. 2, we observe a SH signal of similar levels in the inverted and unpoled regions nearby indicating not just surface domains, but domains inverted towards almost the complete film thickness.

The structures with periods of 1 μm down to 600 nm were analyzed with PFM (the corresponding SH images are provided in the supplementary material). For scanning a full metal Ir/Pt tip (Rocky Mountain Nanotechnology, LLC) with a tip apex of about 30 nm was used. The measurement was performed in resonance-enhanced PFM with an AC signal

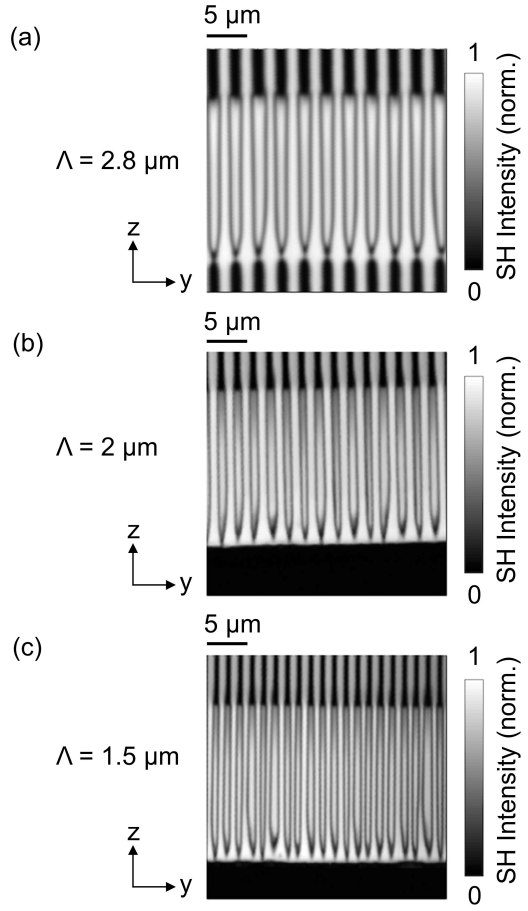

FIG. 2. Typical SH images of poled samples with 2.8 μm (a), 2 μm (b), and 1.5 μm (c) poling period.

with an amplitude of up to $\pm$ 4 V. For the measurement the long axis of the PFM tip was mounted orthogonal with respect to the z-axis of the crystal as indicated by Fig. 1(d). The measurements of the 1 μm period electrodes show the results obtained in the normal signal channel (buckling motion) driven at an AC frequency of 234 kHz. The signals of the 800 nm and 600 nm period structures were obtained after a change of the cantilever and also show the normal signal channel driven at an AC frequency of 82 kHz. The scan direction was parallel to y-axis of the crystal and the scan speed for all scans was smaller than 1 Hz with step sizes less than 30 nm. Figure 3 shows the PFM and SH images of a 1 μm period electrode structure. Figure 3(a) depicts the measured SH signal, while (b)-(d) show the surface topography (b), PFM amplitude (c) and phase signals (d), respectively. The topography record in Fig. 3(b) shows an otherwise flat surface with only the poling electrodes at the top and the bottom of the image being visible. During the measurement it was noted that the Pt/Ir tip removes the gold layer of the thin poling electrode fingers, so here only a $\sim$ 10 nm surface topography can be seen from Fig. 3(b). This is in agreement with the thickness of the Cr adhesion layer, which appears not to be affected by the scan. In contrast, the 300 nm thick gold probe contact pad is not removed by the tip. The removed gold was pushed by the tip outside of the image frame and did not interfere with the measurement. The PFM phase signal (d) shows a $\sim 180°$ phase shift of the piezoresponse in domains with opposing directions due to the inversion of the piezoelectric tensor in poled regions[29], where color orange and purple represents the unpoled areas and the inverted domains respectively. In contrast, the amplitude signal (c) only shows a contrast sensitive to the domain transitions. This behavior of the PFM amplitude signal is expected[29]. Because when the tip is placed above a domain wall, the piezoresponse signal of two adjacent domains will partly cancel, due to the inversion of the piezoelectric tensor. Further, the measured PFM amplitude signals in the poled and unpoled regions are quite similar [see Fig. 3(c)]. In analogy to the SH contrast mechanism, the PFM amplitude is expected to be reduced if domains of different polarity are stacked vertically[29,30]. From experiments and theory, it has been reported that the PFM amplitude signal can provide a domain depth sensitivity of up to 1.7 μm independent of the ferroelectric material[29,30], which is significantly larger than our film thickness (300 nm). Therefore, the observation of a DW contrast rather than a domain polarity indicates—in agreement with the SH results—that the inverted domains completely extend over the film thickness. Hence, the SH image (a) and PFM amplitude image (c) match well with each other as can be seen by several identical details. (The scanned area in the SH image is shifted by 2 periods to the left, compared to the PFM images, as a result of the manual positioning of samples in different instruments.) It should be noted that our results augment previously-reported PFM results on x-cut LNOI samples, where no PFM phase images were reported, while the PFM amplitude images did show a domain polarity contrast rather than a DW contrast[31,32].

Figure 4 shows the PFM images from electrodes with periods of 800 nm (column on the left) and 600 nm (column on the right), where Figs. 4(e) and (f) are the zoomed-in images generated from the areas enclosed by the white dashed lines in Figs. 4(a) and (b), respectively. As observed before, the phase images [panels (c)-(d)] show a $\sim 180°$ phase shift of the piezoresponse in domains of different polarity, while in the amplitude images [panels (a)-(b)], it is mainly the domain transitions that can be seen. For the 800 nm period structures, we observe a mostly similar PFM amplitude in poled domains as in the unpoled areas. This indicates that the inverted domains do penetrate most of the film thickness as discussed above. For the 600 nm period structures, the amplitude signal of the wide domains is similar to that from the unpoled region, but in the narrow domains only a partly recovered amplitude is observed. While the relatively low amplitude signal measured here may indicate partly inverted domains, on closer inspection, the zoomed-in amplitude image in Fig. 4(e) shows not-completely-recovered signal in the unpoled area compared to the wide inverted domains as well. This can be interpreted as that the width of these narrow structures (< 100 nm) is at the limit of the PFM resolution, which is correlated with the radius of the scanning tip. For bulk single crystalline LN, the estimated lateral resolution for the metallic tip used here (radius $\approx$ 30 nm) is around 36 nm[29]. The images of the 800 nm electrode show domain structures of the targeted period, with each

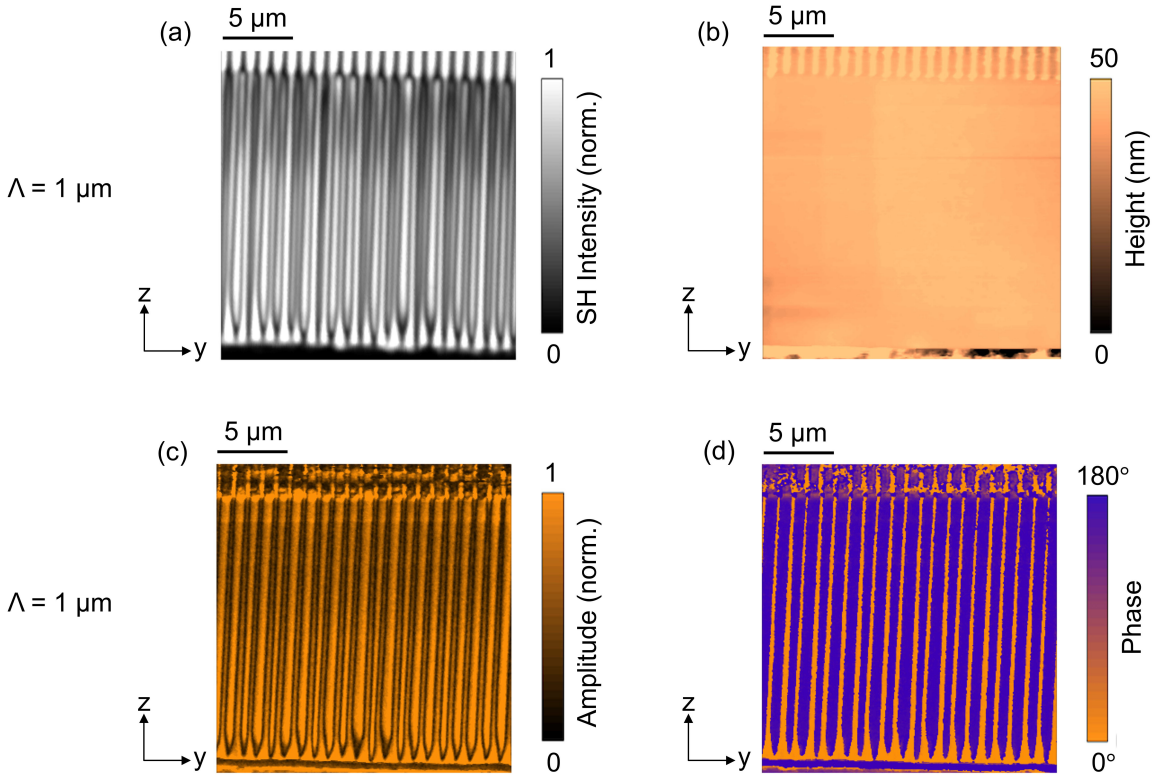

FIG. 3. SH image (a), surface topography (b), PFM amplitude (c) and phase (d) images of a poled sample with 1 μm period.

domain reaching the ground electrode. The domain structures with 600 nm period show an interesting behavior, where every second domain only propagate to about the middle of the poling gap, leading to a pattern with an effectively doubled period (compared to the designed period) in the area near the ground electrode. A closer inspection of the 1 μm and 800 nm period structures already indicates that approximately every second domain is slightly narrower than the two respective neighboring domains. This behavior is observed in all our poling experiments of the submicron-period structures, and is progressively more pronounced with smaller periods, which could only be partly compensated by optimizing the poling pulse form. Therefore, a systematic interaction of domains is indicated for further study from a physics perspective.

From literature, it is well established that DWs in LN, as well as other ferroelectrics, are accompanied with various effects[33,34], such as strain[35,36], charges and electric fields[37,38]. While the length scale of domain transition (defined as the change of sign of spontaneous polarization) is measured and predicted to be on the order of a few unit cells[33,39–43], the accompanying effects, such as strain fields and electric fields, have been observed to expand over a wide range varying from a nanometer to several microns around the DWs[33,34,44]. In agreement with these length scales, we observe an interaction of neighboring domains with periods of 1 μm and less. Interestingly, we do not just observe a random pattern of domains, but rather structures with a double periodicity, where every second domain grows at the cost of its two neighbors. Recently, periodic and quasi-periodic patterns on sub-micron scales have been observed in domains written by biased scanning probe microscopy (SPM) tips in polar (z-cut) and non-polar cuts (x- and y-cut) of bulk LN[45,46]. In a similar manner to our experiment, for large domain spacing, uniform domain chains were formed with SPM writing, while as the distance between the adjacent bias application locations gets smaller, domains of non-equal sizes with a double periodicity were observed. By further decreasing the domain spacing, domains with a triple periodicity and eventually quasi-periodic and non-periodic patterns were formed[45]. The origin of these behaviors is believed to be domain-domain interactions through electrostatic and strain fields, and a theoretical model was developed to generate the phase diagram of the domain switching behaviors[45]. More importantly, according to Ref. [45], transitions of these domain patterns from uniform chains to period doubling structures, and then to quasi-periodic structures can be achieved by varying the poling temperature or the relative humidity at the sample surface. As is shown in Figs. 4(b) and (f), domains with DW-DW distances less than 200 nm have already been fabricated by simply adjusting the poling pulse height and length. This suggests that uniform domain structures with even smaller periodicities could be formed with improved control of the poling pulse as well as the poling environment. Other possible approaches to further improve the poling uniformity include using multiple poling pulses[31,47], poling differently doped LN to support the pinning of domain structures, and UV light-assisted poling[48,49]. Indeed, the domain to domain interactions are not yet very well understood in TFLN and require further investigation, in

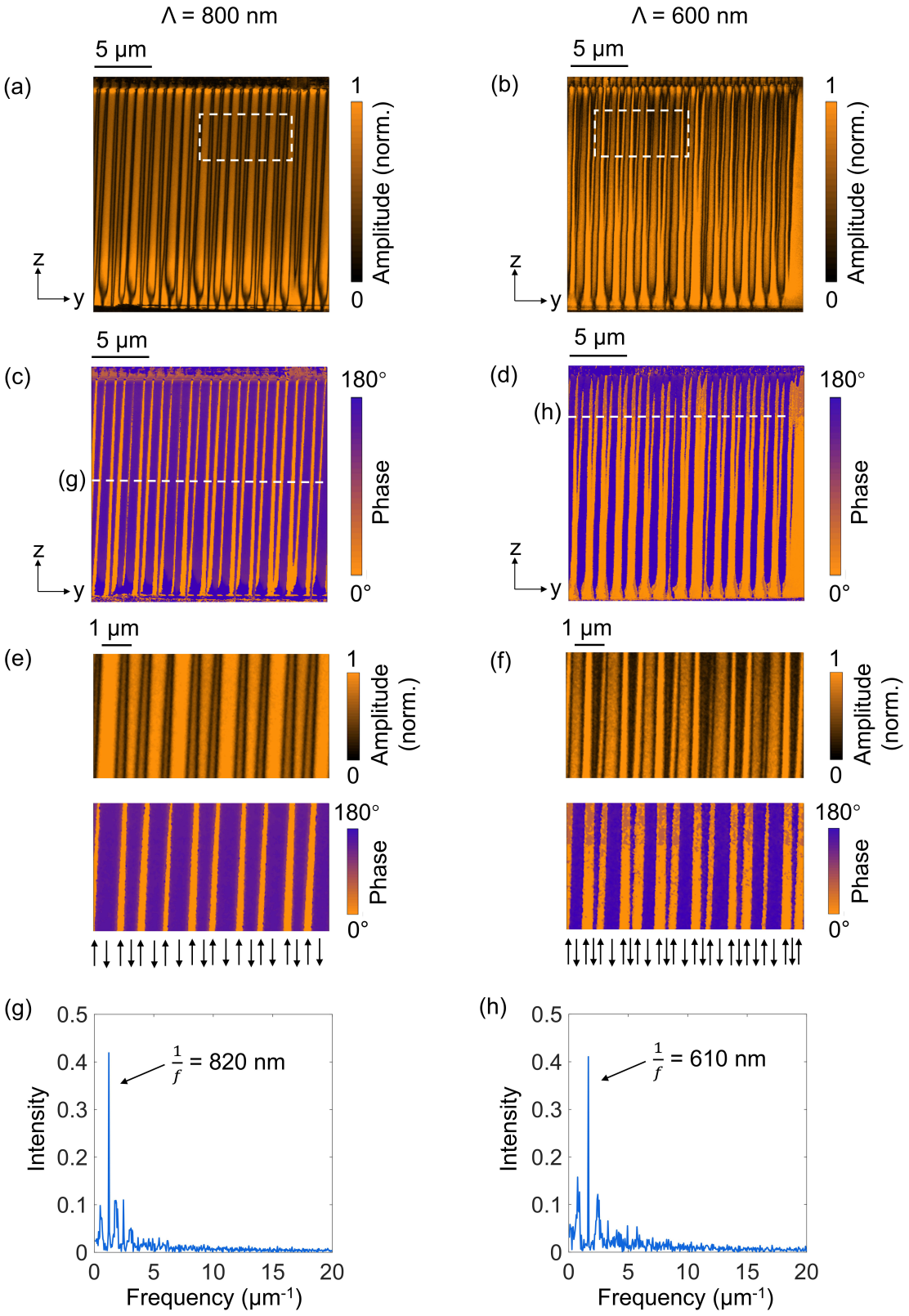

FIG. 4. (a)-(d) PFM amplitude and phase images of structures with a poling period of 800 nm (column on the left) and 600 nm (column on the right). (e) and (f) Zoomed-in PFM amplitude (top panel) and phase (bottom panel) images for the 800 nm and 600 nm period structures obtained from the areas enclosed by the white dashed lines shown in panels (a) and (b); Arrows on the bottom indicate the orientation of spontaneous polarization of TFLN, where upward and downward arrows represent the un-inverted and inverted domains, respectively. (g) and (h) Fourier spectrum of the PFM phase data acquired from the region shown with the white dashed lines in panels (c) and (d); f is the spatial frequency, in unit of $\mu\mathrm{m}^{-1}$.

which Kelvin probe force microscopy could be used to image and visualize space charge distributions around the DWs[46].

It should be noted that while for the 600 nm period electrodes only every second domain reaches the ground electrode, periodic structures with the designed parameters are still present close to the positive electrode, as is shown in Figs. 4(f) and (h). To obtain a quantitative estimate of the achieved periodicity, we calculated the Fourier transform of the PFM phase data line scan, acquired from the slices indicated by the white dashed lines shown in Figs. 4(c) and (d); similar studies have been performed in Ref. [31], for example. The Fourier spectra from the two line-scans are shown in Figs. 4(g) and (h), which show a main period of 820 nm and 610 nm with the peak amplitude being 0.42 and 0.41 respectively. The calculated peak amplitude here is slightly reduced from the ideal value of 0.64 $[(2/\pi)\sin(\pi/2)]$, which is the leading coefficient in the Fourier series for a periodic square-wave function with 50% duty cycle. The period doubling behavior of the switched domains appears as the side lobes in the Fourier spectra. The calculated duty cycle from these two line-scans are 67.7% $\pm$ 9.1% and 54.3% $\pm$ 12.4% respectively. Though the uniformity of the domain structures here is not as good as that of the larger periods, due to the speculated domain interactions, the results still demonstrate a fairly uniform domain grid comparable to structures used in the reported efficient nonlinear devices[17]. Note that the width of the poling region here is 20 μm, while typical fundamental TE mode in TFLN waveguides only extends to less than 5 μm (in the z direction)[18–20]. Even for the 600 nm period structures poled here, there still appears to be adequate space to fabricate optical waveguides where the period is well reproduced, as is shown in Figs. 4(f) and (h).

All the fabricated domain structures have been stable for at least eight months between the initial poling, SH imaging and the subsequent PFM analysis. Using a 2.8 μm QPM periodicity, we have fabricated 5 mm long periodically-poled waveguides which were used as sources of entangled photon pairs at telecommunications wavelengths[26]. Because the test chips reported here contained a large number of poled structures of relatively short length in order to explore the parameter space, we have not yet fabricated optical waveguide structures with the shorter QPM dimensions. However, we do not see a fundamental limitation in the development of optical waveguides that are at least several millimeters in length using the same poling protocol.

IV. CONCLUSION

We have studied and demonstrated poling of x-cut TFLN with periods varying from 2.8 μm to 600 nm, using the lithographically-structured electrodes and single voltage pulses. SH microscopy and PFM were used to inspect the domain structures, which show domain grids with periods down to 600 nm, and features with sizes less than 200 nm. We observed period doubling behaviors in the sub-micron period structures formed by domain interactions, which is progressively more pronounced with smaller periods. Further improvements in the domain uniformity with even smaller periods can be expected by optimizing the poling temperature or environment humidity. Our work shows that the same poling protocol can be used to fabricate domain grids with periods over a wide range, through only slight modifications in the poling waveform, which provides one key step towards the realization of thin-film PPLN based nonlinear devices, such as mirrorless OPO.

SUPPLEMENTARY MATERIAL

See the supplementary material for detailed information for the poling setup, poling waveform optimization, simulated SH signatures and SH images for the sub-micron period domains.

ACKNOWLEDGMENTS

This work was funded through Sandia National Laboratories (SIGMA-NONLin Project) and the National Science Foundation (NSF) (EFMA-1640968). Further, the authors would like to thank the Deutsche Forschungsgemeinschaft (DFG) (EN 434/41-1 and EN 434/40-1) and Volkswagen Foundation (Volkswagen Stiftung, 90261) for partly funding this work.

DATA AVAILABILITY

The data that support the findings of this study are available from the corresponding author upon reasonable request.

REFERENCES

[1] C. Canalias and V. Pasiskevicius, Nat. Photonics **1**, 459 (2007).
[2] A. Christ, A. Eckstein, P. J. Mosley, and C. Silberhorn, Opt. Express **17**, 3441 (2009).
[3] A. Boes, V. Sivan, G. Ren, D. Yudistira, S. Mailis, E. Soergel, and A. Mitchell, Appl. Phys. Lett. **107**, 022901 (2015).
[4] S. Grilli, P. Ferraro, L. Sansone, M. Paturzo, and P. De Natale, Ferroelectrics **352**, 72 (2007).
[5] A. C. Busacca, C. L. Sones, V. Apostolopoulos, R. W. Eason, and S. Mailis, Appl. Phys. Lett. **81**, 4946 (2002).
[6] M. Minakata, M. S. Islam, S. Nagano, S. Yoneyama, T. Sugiyama, and H. Awano, Solid-State Electronics **50**, 848 (2006).
[7] C. Canalias, V. Pasiskevicius, R. Clemens, and F. Laurell, Appl. Phys. Lett. **82**, 4233 (2003).
[8] C. Canalias, V. Pasiskevicius, and F. Laurell, Ferroelectrics **340**, 27 (2006).
[9] A. Zukauskas, A.-L. Viotti, C. Liljestrand,V. Pasiskevicius, and C. Canalias, Sci. Rep. **7**, 8037 (2017).
[10] R. S. Coetzee, A. Zukauskas, C. Canalias, and V. Pasiskevicius, APL Photonics **3**, 071302 (2018).
[11] R. L. Sutherland, in *Handbook of Nonlinear Optics* (CRC Press, 2003) pp. 295–323.
[12] G. Ghione, in *Semiconductor Devices for High-Speed Optoelectronics* (Cambridge University Press, 2009) pp. 356–439.
[13] R. S. Weis and T. K. Gaylord, Appl. Phys. A **37**, 191 (1985).
[14] M. Schröder, A. Haußmann, A. Thiessen, E. Soergel, T. Woike, and L. M. Eng, Adv. Funct. Mater. **22**, 3936 (2012).
[15] K. Buse, A. Adibi, and D. Psaltis, Nature **393**, 665 (1998).

[16] A. Bartasyte, S. Margueron, T. Baron, S. Oliveri, and P. Boulet, Adv. Mater. Interfaces **4**, 1600998 (2017).
[17] L. Chang, Y. Li, N. Volet, L. Wang, J. Peters, and J. E. Bowers, Optica **3**, 531 (2016).
[18] A. Rao, M. Malinowski, A. Honardoost, J. R. Talukder, P. Rabiei, P. Delfyett, and S. Fathpour, Opt. Express **24**, 29941 (2016).
[19] A. Rao, K. Abdelsalam, T. Sjaardema, A. Honardoost, G. F. Camacho-Gonzalez, and S. Fathpour, Opt. Express **27**, 25920 (2019).
[20] C. Wang, C. Langrock, A. Marandi, M. Jankowski, M. Zhang, B. Desiatov, M. M. Fejer, and M. Lončar, Optica **5**, 1438 (2018).
[21] P. O. Weigel and S. Mookherjea, J. Opt. Soc. Am. B **35**, 593 (2018).
[22] M. Rüsing, P. O. Weigel, J. Zhao, and S. Mookherjea, IEEE Nanotechnol. Mag. **13**, 18 (2019).
[23] T. R. Volk, R. V. Gainutdinov, and H. H. Zhang, Appl. Phys. Lett. **110**, 132905 (2017).
[24] J. Lu, J. B. Surya, X. Liu, A. W. Bruch, Z. Gong, Y. Xu, and H. X. Tang, Optica **6**, 1455 (2019).
[25] P. Mackwitz, M. Rüsing, G. Berth, A. Widhalm, K. Müller, and A. Zrenner, Appl. Phys. Lett. **108**, 152902 (2016).
[26] J. Zhao, C. Ma, M. Rüsing, and S. Mookherjea, Phys. Rev. Lett. **124**, 163603 (2020).
[27] J. Zhao, M. Rüsing, and S. Mookherjea, Opt. Express **27**, 12025 (2019).
[28] M. Rüsing, J. Zhao, and S. Mookherjea, J. Appl. Phys. **126**, 114105 (2019).
[29] E. Soergel, J. Phys. D: Appl. Phys. **44**, 464003 (2011).
[30] F. Johann, Y. J. Ying, T. Jungk, Á. Hoffmann, C. L. Sones, R. W. Eason, S. Mailis, and E. Soergel, Appl. Phys. Lett. **94**, 172904 (2009).
[31] J. T. Nagy and R. M. Reano, in *Frontiers in Optics/Laser Science* (2019) p. JTu3A.10.
[32] J. T. Nagy and R. M. Reano, Opt. Mater. Express **9**, 3146 (2019).
[33] V. Gopalan, V. Dierolf, and D. A. Scrymgeour, Annu. Rev. Mater. Res. **37**, 449 (2007).
[34] M. Rüsing, S. Neufeld, J. Brockmeier, C. Eigner, P. Mackwitz, K. Spychala, C. Silberhorn, W. G. Schmidt, G. Berth, A. Zrenner, and S. Sanna, Phys. Rev. Mater. **2**, 103801 (2018).
[35] T. Jach, S. Kim, V. Gopalan, S. Durbin, and D. Bright, Phys. Rev. B **69**, 064113 (2004).
[36] Kh. Hassani, M. Sutton, M. Holt, Y. Zuo, and D. Plant, J. Appl. Phys. **104**, 043515 (2008).
[37] V. Dierolf and C. Sandmann, J. Lumin. **102-103**, 201 (2003).
[38] V. Dierolf and C. Sandmann, Appl. Phys. B **78**, 363 (2004).
[39] C.-L. Jia, S.-B. Mi, K. Urban, I. Vrejoiu, M. Alexe, and D. Hesse, Nat. Mater. **7**, 57 (2008).
[40] Y. B. Chen, M. B. Katz, X. Q. Pan, R. R. Das, D. M. Kim, S. H. Baek, and C. B. Eom, Appl. Phys. Lett. **90**, 072907 (2007).
[41] J. Padilla, W. Zhong, and D. Vanderbilt, Phys. Rev. B **53**, R5969 (1996).
[42] B. Meyer and D. Vanderbilt, Phys. Rev. B **65**, 104111 (2002).
[43] D. A. Scrymgeour, V. Gopalan, A. Itagi, A. Saxena, and P. J. Swart, Phys. Rev. B **71**, 184110 (2005).
[44] S. Kim and V. Gopalan, Mater. Sci. Eng., B **120**, 91 (2005).
[45] A. V. Ievlev, S. Jesse, A. N. Morozovska, E. Strelcov, E. A. Eliseev, Y. V. Pershin, A. Kumar, V. Ya. Shur, and S. V. Kalinin, Nat. Phys. **10**, 59 (2014).
[46] A. Turygin, D. Alikin, Y. Alikin, and V. Shur, Materials **10**, 1143 (2017).
[47] M. Younesi, P. Kumar, B. J. Stanicki, R. Geiss, W.-K. Chang, Y.-H. Chen, F. Setzpfandt, and T. Pertsch, in *CLEO Europe and EQEC* (2019) p. ck_8_4.
[48] H. Steigerwald, F. von Cube, F. Luedtke, V. Dierolf, and K. Buse, Appl. Phys. B **101**, 535 (2010).
[49] C. L. Sones, A. C. Muir, Y. J. Ying, S. Mailis, R. W. Eason, T. Jungk, Á. Hoffmann, and E. Soergel, Appl. Phys. Lett. **92**, 072905 (2008).

(a)

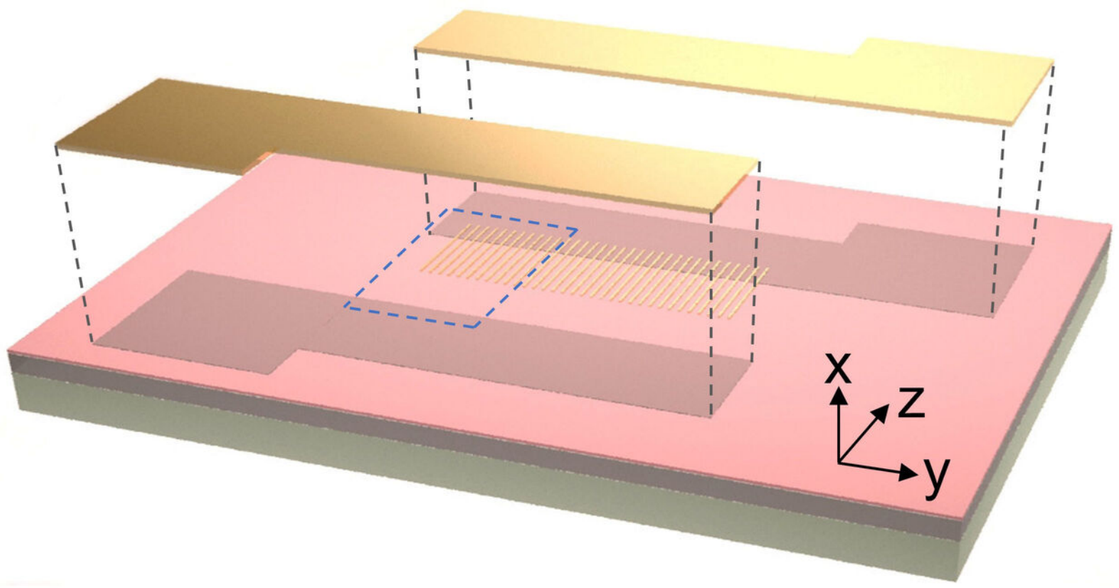
x
z
y

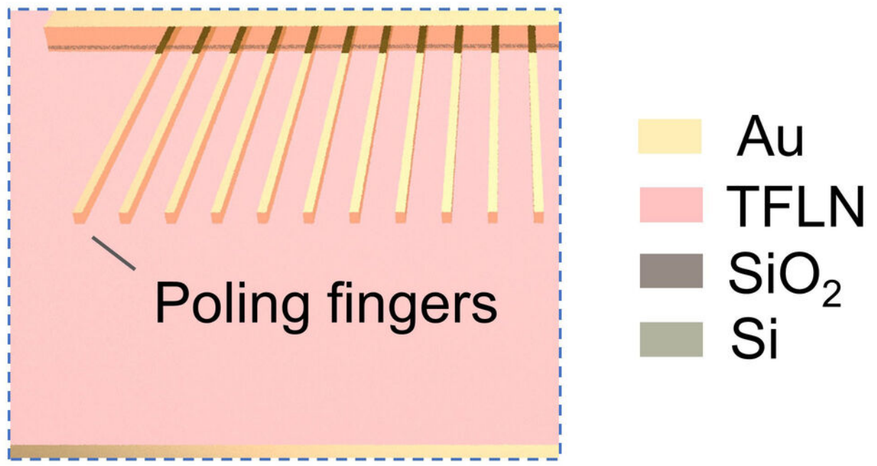
Poling fingers
Au
TFLN
SiO2
Si

(b)

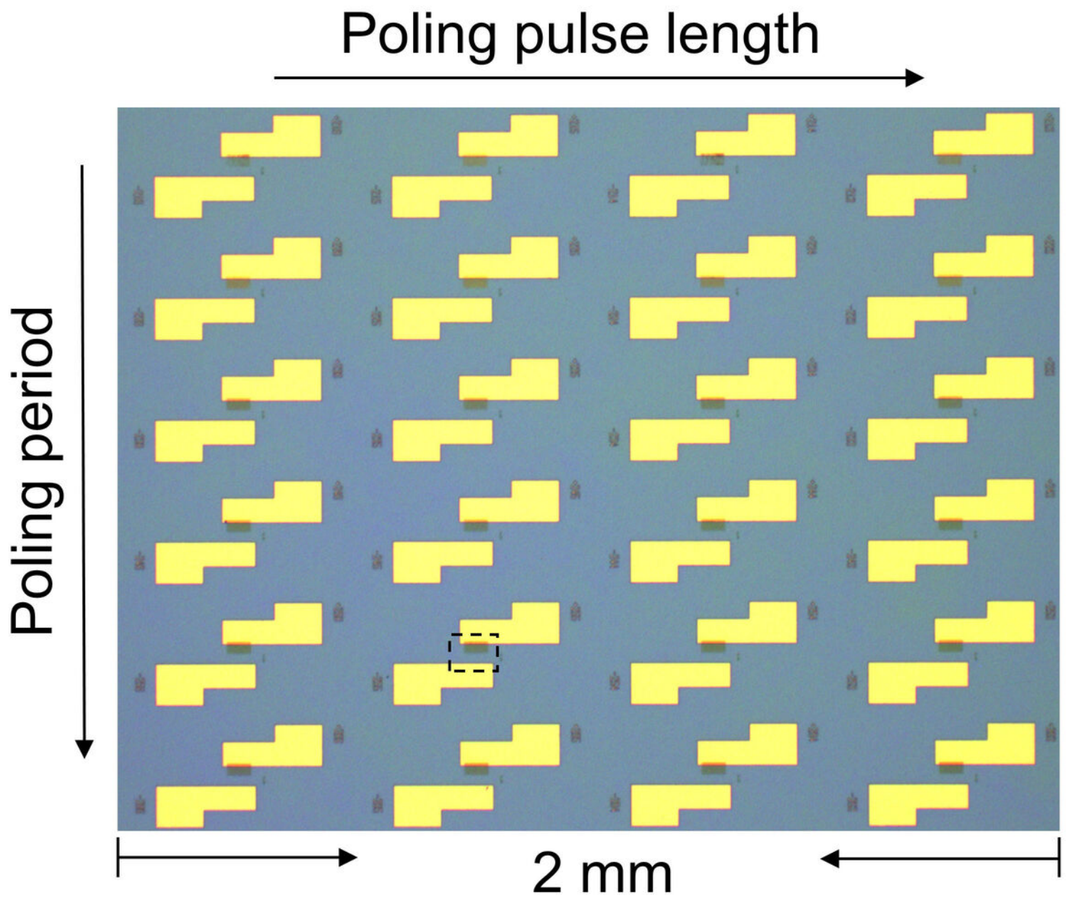
Poling pulse length
Poling period
2 mm

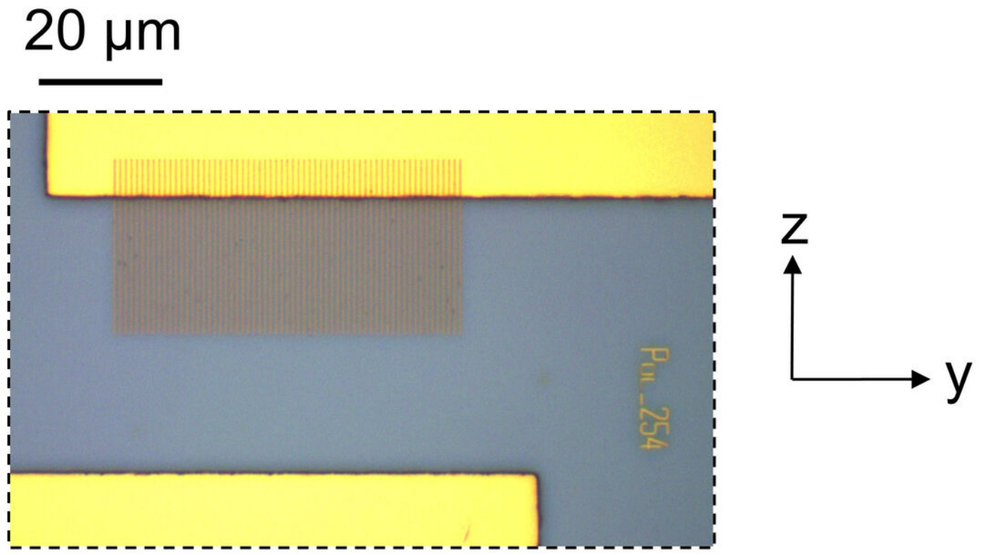
20 μm
z
y

(c)

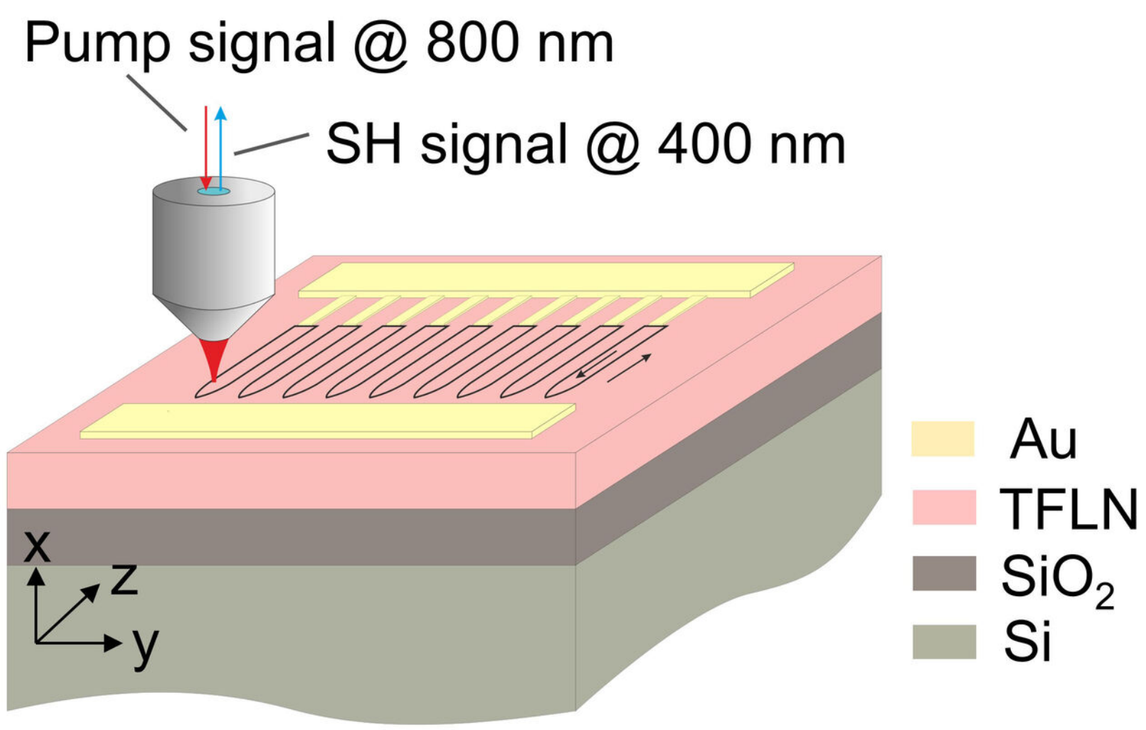
Pump signal @ 800 nm
SH signal @ 400 nm
x
z
y
Au
TFLN
SiO2
Si

(d)

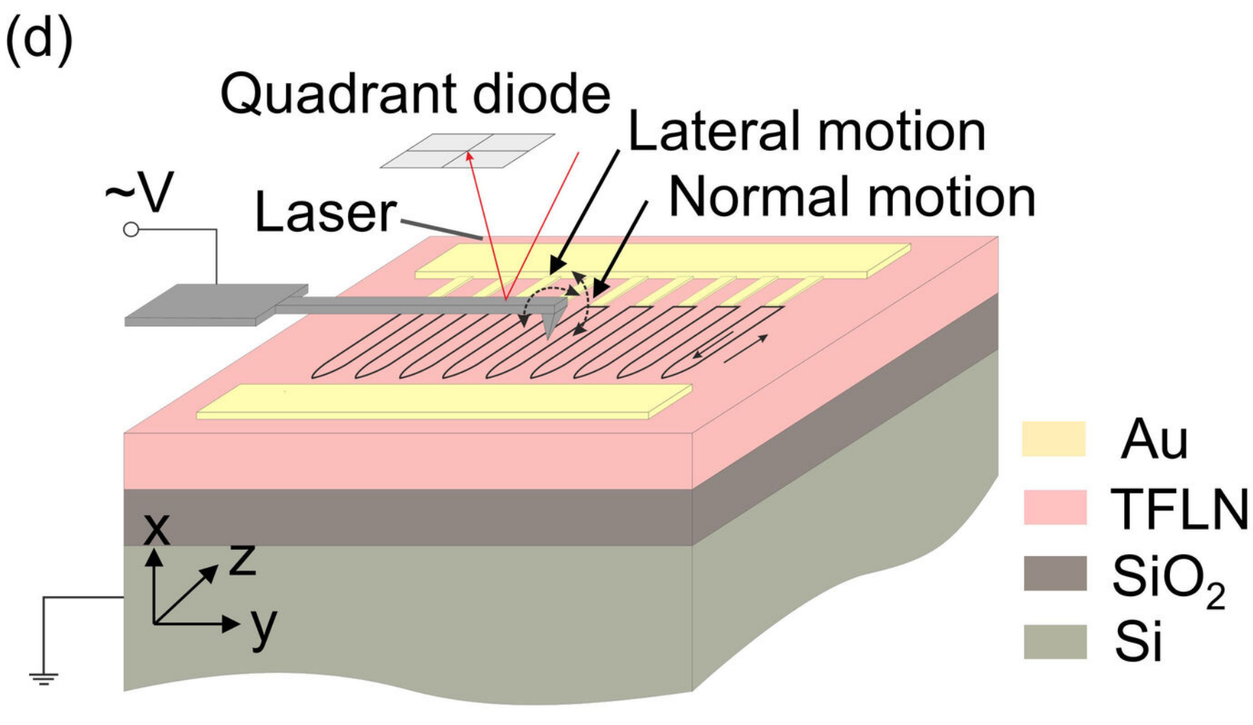
Quadrant diode
Lateral motion
Normal motion
~V
Laser
x
z
y
Au
TFLN
SiO2
Si

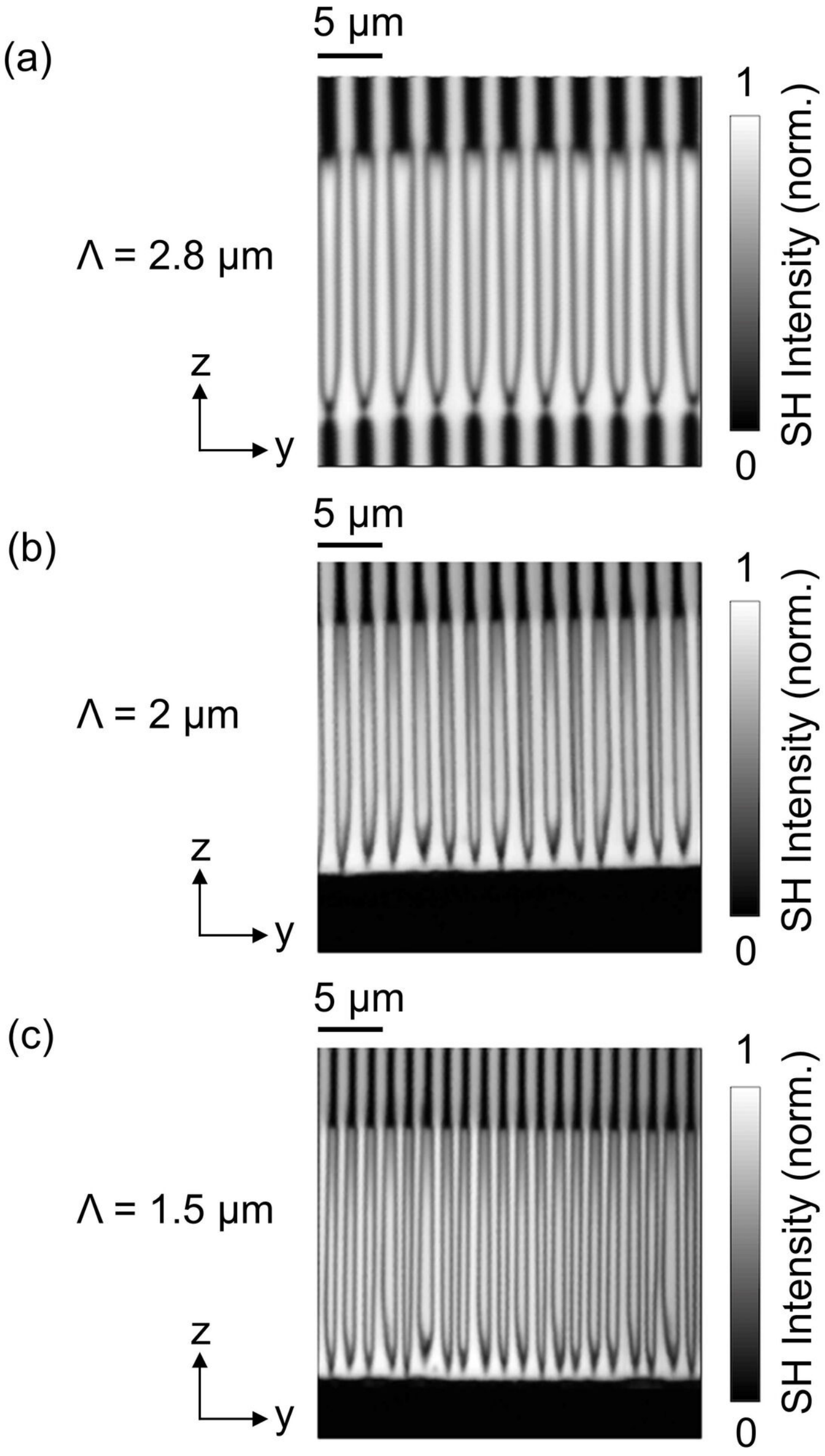
(a)
5 μm
Λ = 2.8 μm
z
y
1
0
SH Intensity (norm.)
(b)
5 μm
Λ = 2 μm
z
y
1
0
SH Intensity (norm.)
(c)
5 μm
Λ = 1.5 μm
z
y
1
0
SH Intensity (norm.)

(a)

5 μm

Λ = 1 μm

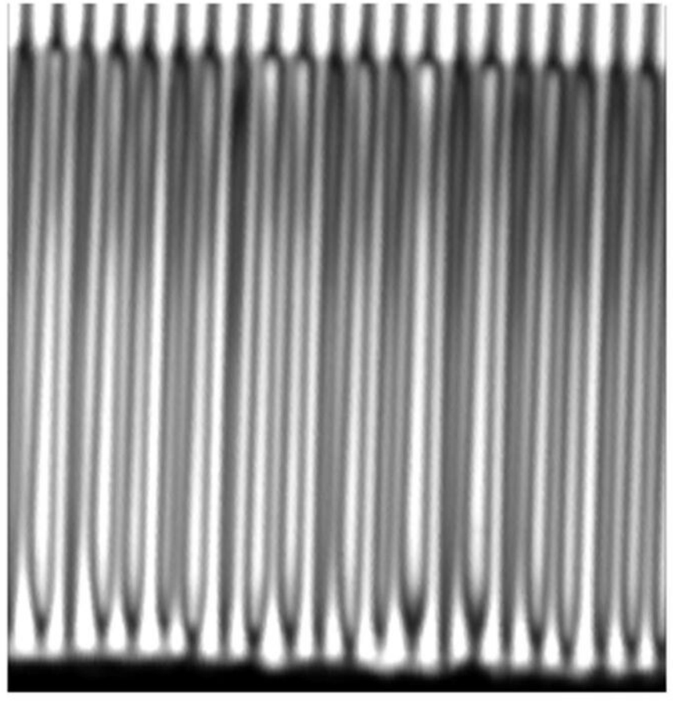

z

y

1

0

SH Intensity (norm.)

(b)

5 μm

z

y

50

0

Height (nm)

(c)

5 μm

Λ = 1 μm

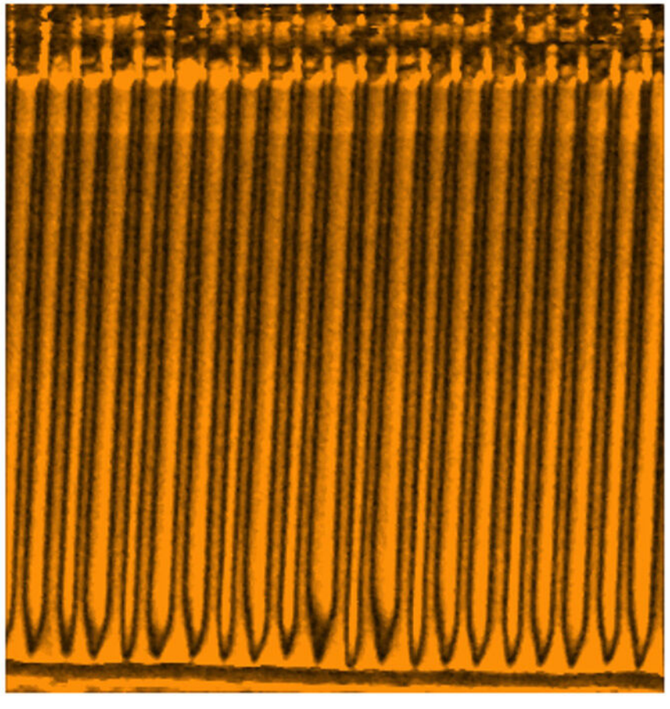

z

y

1

0

Amplitude (norm.)

(d)

5 μm

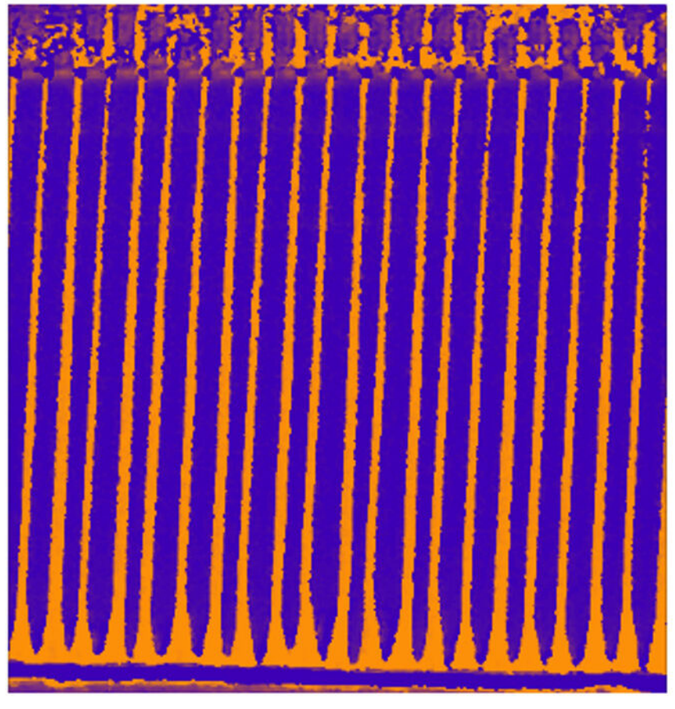

z

y

180°

0°

Phase

Λ = 800 nm

Λ = 600 nm

(a)

(b)

(c)

(d)

(e)

(f)

(g)

(h)

5 μm

1 μm

z

y

1

0

Amplitude (norm.)

180°

0°

Phase

(g)

(h)

0.5

0.4

0.3

0.2

0.1

0

Intensity

$\frac{1}{f}$ = 820 nm

$\frac{1}{f}$ = 610 nm

0

5

10

15

20

Frequency (μm^{-1})